IEEE Access
Multidisciplinary | Rapid Review | Open Access Journal

Received October 30, 2019, accepted November 14, 2019, date of current version November 27, 2019.

Digital Object Identifier 10.1109/ACCESS.2019.2954343

Pattern-Reconfigurable Antenna With Switchable Wideband to Frequency-Agile Bandpass/Bandstop Filtering Operation

SEYED-ALI MALAKOOTI, (Student Member, IEEE), AND CHRISTOPHE FUMEAUX, (Fellow, IEEE)
School of Electrical and Electronics Engineering, The University of Adelaide, Adelaide, SA 5005, Australia

Corresponding author: Seyed-Ali Malakooti (seyedali.malakooti@adelaide.edu.au)

This work was supported by the Australian Research Council under Discovery Project under Grant DP160103039.

ABSTRACT A three-element antenna system with the ability to operate in a unique set of switchable and frequency-tunable configurations is presented here. Firstly, this antenna system can switch between sum and difference radiation patterns using a mirrored arrangement of antenna feeding lines that bypasses the need for an additional phase inverter. Secondly, the frequency response of this antenna can be switched between three states of operation, namely wideband, tunable bandpass, and tunable bandstop characteristics. Importantly, the pattern reconfigurability function can be generated in all three states of the frequency-agile response. To realize this extended set of selectable functionalities, a three-state filter and a switchable power divider are used to feed a triple-element quasi-Yagi-Uda antenna array. The proposed system is experimentally validated, demonstrating sum and difference patterns over a measured 79.8% fractional bandwidth for the wideband state of operation, and a tunability of 51.3% for the bandpass state and 50.3% for the bandstop state.

INDEX TERMS Cognitive radio, pattern reconfigurability, switchable wideband to tunable filtering antenna.

I. INTRODUCTION

Spectrum scarcity due to the exhaustive utilization of available frequency bands by licensed users motivates the development of reconfigurable antennas for cognitive radio systems. Various antennas with frequency agility [1]–[5], pattern reconfigurability [6]–[9], polarization reconfigurability [10]–[13] and combinations of these modalities [14]–[19] have been proposed recently to accommodate this need. According to [20], three states of operation are required to observe and react to the spectrum utilization in cognitive radio systems. First, a wideband state, which is used to scan the frequency spectrum for finding unoccupied frequencies. Second, a tunable narrowband state to allocate an idle frequency to a primary user. Third, a tunable notch-band state to allocate a wideband spectrum to a secondary user without any interference with the already occupied frequency band. For hardware implementation, a number of wideband to discretely tunable narrowband [21]–[24] and wideband to continuously tunable narrowband antenna structures [25]–[29] have been presented. More recently, some tunable bandpass-to-bandstop antennas have been proposed in [30], [31]. However, an essential functionality of cognitive radio systems, namely the wideband operation state was missing in these realizations. To the best of the authors' knowledge, no system implementing all these three operation states in a single reconfigurable structure has hitherto been reported.

Pattern diversity is also a useful feature for cognitive radio systems for wider space signal coverage and multipath fading mitigation. To meet this requirement, dual-input antennas with sum and difference pattern diversity have widely been explored in [31]–[35]. In these studies, the use of a microwave comparator generating in-phase and out-of-phase input signals was inevitable, leading to a relatively high complexity of the overall system. As an alternative, aiming at lowering the complexity, the design presented in [36] employed a planar structure with electrically switchable sum and difference patterns for narrowband operation and circular polarization. A wider band design was presented in [37], where sum and difference patterns were switched using a phase-inversion feeding network in a three dimensional structure.

In this paper, we are aiming at realizing three different frequency states of cognitive radio systems combined with a low complexity pattern diversity function in a single antenna system. To this end, a switchable and tunable filter is integrated with a switchable three-output power divider

The associate editor coordinating the review of this manuscript and approving it for publication was Nagendra Prasad Pathak.

and a triple-element quasi-Yagi-Uda antenna with in-built phase inverter, as shown in Fig. 1. The filter generates three different states of switchable allpass to tunable bandpass and tunable bandstop functionalities. The switchable power divider excites two antenna elements at a time and keeps the third element inactive. When the input signal is split into the leftmost output branches of the power divider, a sum directive radiation pattern is generated. In contrast, a difference beam radiation pattern with a null in its boresight direction is generated when the input signal is split into the two rightmost output ports of the power divider. The 3D models of the two different beams are illustrated in Fig. 2a and Fig. 2b. Contrary to the reported designs in the open literature, there is no need for a microwave comparator and external phase inverter to generate the sum and difference radiation patterns. The only drawback of that simpler arrangement is that the two radiation pattern functionalities are achieved sequentially. There are three distinct novel aspects to this design:

1) The allpass state of operation has been added to our previously published filter in [31]. This means that the enhanced filter features an allpass state which can be switched to a bandpass state and to a bandstop state, both with tunable operating frequencies.
2) Switchable sum and difference radiation patterns are realized by exploiting in-built phase inversion function in the mirror arrangement of the rightmost antenna feeding structure. This sequential pattern switching is in contrast to our presented design in [31] where a double-input antenna and an external coupler were used to generate simultaneous sum and difference pattern diversity.
3) A unique combination of functionalities in a single antenna system is demonstrated, including the switchable generation of sum and difference patterns over 79.8% bandwidth, 51.3% bandpass tuning range, and 50.3% bandstop tuning range.
4) Compared to the design in [31], this structure eliminates the requirement for a prohibitive external coupler and facilitates the integration of a single filter structure as opposed to two filters necessary in [31], thereby reducing the cost and complexity of the overall system while offering additional states of reconfigurability.

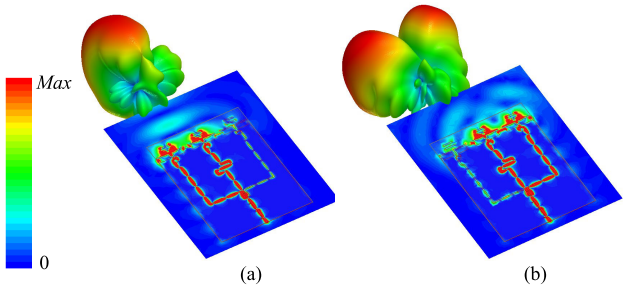

FIGURE 2. Instantaneous E-field distribution and generated radiation pattern for (a) the sum beam configuration, and (b) the difference beam configuration.

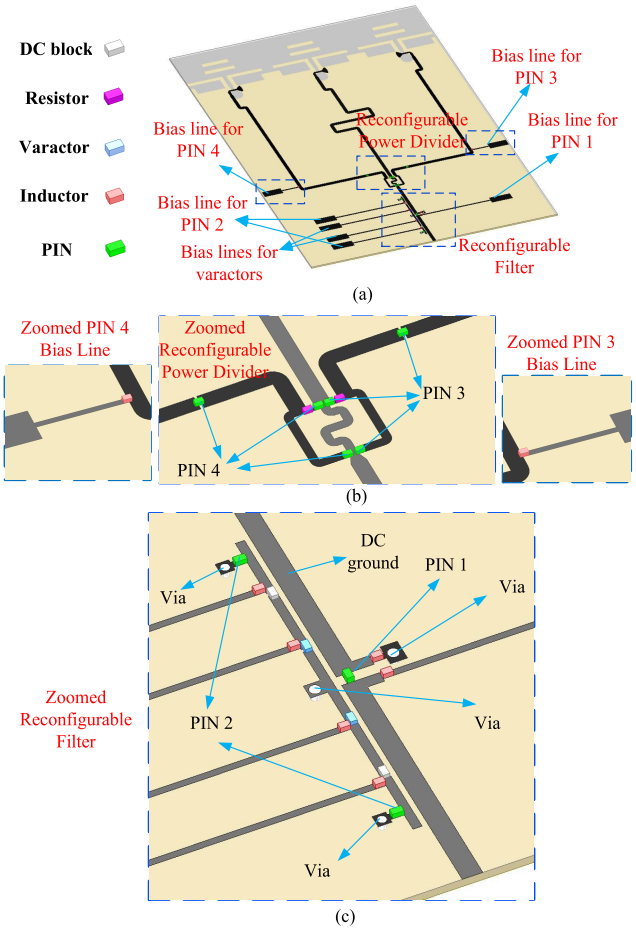

FIGURE 1. (a) Proposed antenna system structure. (b) Magnified reconfigurable power divider section in conjunctions with bias lines for its PIN diodes. (c) Magnified reconfigurable filter.

II. ANTENNA SYSTEM DESIGN

A three-dimensional view of the antenna system is illustrated in Fig. 1a, comprising a triple-element antenna, a reconfigurable power divider (magnified in Fig. 1b) and a reconfigurable filter (magnified in Fig. 1c). The antenna elements excited by the power divider will enable pattern diversity over a wideband frequency, while feeding this structure by the switchable and tunable filter helps generate three states of wideband, tunable bandpass and tunable bandstop operation. Hence, the combination of these three circuits brings about a unique functionality that has not been reported in the open literature thus far. All the required lumped components and bias lines are included in these representations. The PIN diodes are all MACOM MA4FCP300 diodes [38] with an equivalent OFF state simulation model of 20 KΩ resistance and 0.04 pF shunt capacitance, while the ON state simulation model is purely resistive with 4 Ω resistance. The varactor diodes in this design are MACOM MA46H120 [39] with a simulation equivalent model of a varying capacitance from 0.15 pF to 1.30 pF connected to a series resistance of 1.6 Ω and a

series inductance of 0.05 nH. The resistors are 0402 surface mount resistors with 100 Ω resistance. The used RF choke inductors are Murata LQW15AN15NG00 [40] with 15 nH inductance, and the utilized DC block capacitor models are GRM0332C1H100JA01 [41] with 10 pF capacitance. All the constituents of the antenna system described in this section are integrated and printed on a Rogers RO4003C substrate with a relative permittivity of 3.38, loss tangent of 0.0027, and thickness of 0.8128 mm. The next three subsections elaborate on the building blocks of this antenna system and their simulated functionalities. All the simulations are conducted using HFSS in Ansys Electronics Desktop software.

A. TRIPLE-ELEMENT ANTENNA

The quasi-Yagi-Uda antenna structure in [42] is adopted as individual antenna element with some modifications in the feeding lines and the operating frequency. The structure presented in [42] is an ultrawideband and compact quasi-Yagi-Uda antenna element which is an ideal choice for developing arrays of several elements. This is because the compact size of the antenna in terms of wavelength allow a sufficiently close packing of the elements, which prevents the appearance of grating lobes at higher frequencies, while the remaining separation between the antenna elements keeps the mutual coupling to an acceptable level. The triple-element quasi-Yagi-Uda antenna configuration (without the reconfigurable power divider and the reconfigurable filter) is shown in Fig. 3a with the annotated dimensions tabulated in Table 1. The middle transmission line feed for the central element is meandered to have the same electrical length as the lateral feeding transmission lines. Importantly, for the pattern reconfiguration, the rightmost feeding line is mirrored with respect to the other two feeding lines to generate an intrinsic and frequency independent 180° phase difference between the middle and rightmost antenna elements. Although the fundamental antenna elements are the same as in [31], three antenna elements are required to enable additional functionality in this article, as opposed to the two antenna elements excited by an external coupler in [31]. The third antenna element is used to facilitate pattern switchability and obviate the need for lossy and expensive external coupler by providing inherent and frequency-independent phase inversion.

TABLE 1. Dimension values of the proposed antenna system.

par.	value (mm)	par.	value (mm)	par.	value (mm)	par.	value (mm)
W_1	1.8	L_2	73.2	L_{12}	7.4	L_{22}	7.9
W_2	2.2	L_3	10.8	L_{13}	20.5	L_{23}	6.2
W_3	2.2	L_4	4.3	L_{14}	17.4	L_{24}	22.0
W_4	0.9	L_5	27.2	L_{15}	14.9	L_{25}	3.3
W_5	1.4	L_6	10.7	L_{16}	16.0	L_{26}	10.3
W_6	1.0	L_7	23.2	L_{17}	4.5	D_1	7.0
W_7	0.8	L_8	5.0	L_{18}	18.5	D_2	1.0
W_8	1.8	L_9	20.0	L_{19}	4.1	D_3	0.8
W_9	1.0	L_{10}	10.8	L_{20}	6.5		
L_1	34.5	L_{11}	5.1	L_{21}	3.0		

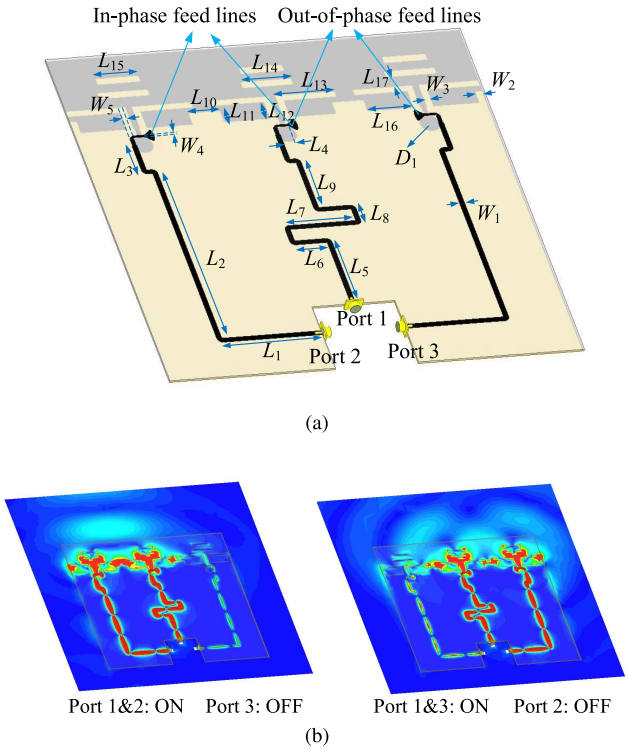

FIGURE 3. Proposed three-element antenna structure. (a) 3D view with in-built in-phase and out-of-phase feed lines and related dimensions. (b) Instantaneous E-field distribution when two ports are excited and one port is inactive.

The working principle of this antenna system is illustrated in Fig. 3b where it can be observed that only two elements are contributing to the radiation at a particular time, with the third element remaining inactive. As shown on the left-hand side of Fig. 3b, when Port 1 and Port 2 are excited by an in-phase signal and Port 3 is inactive, the electric fields of the two leftmost antennas are combined constructively in endfire direction, thereby generating a sum radiation pattern. By contrast, when Port 1 and Port 3 are excited by an in-phase signal and Port 2 is inactive, the electric fields of the two rightmost antennas are combined destructively in the endfire direction due to their mirrored input transmission lines, thereby generating a difference radiation pattern.

The simulated scattering parameters of these antennas are illustrated in Fig. 4b. The reflection coefficients for all the input ports are the same and remain below −10 dB in the range of 2.52 GHz to 6.24 GHz. This wide bandwidth of the antenna elements will be exploited for the three-state filtering functions of the overall antenna system. Within this band, the isolation between Port 1 and Port 2 is below −16 dB and the isolation between Port 2 and Port 3 is below −22 dB. It is noteworthy that the simulated efficiency of this triple-element antenna by itself is around 94%. This further confirms that this antenna is an appropriate element choice for our antenna system design in which the reconfigurable feeding network is the main source of inevitable loss.

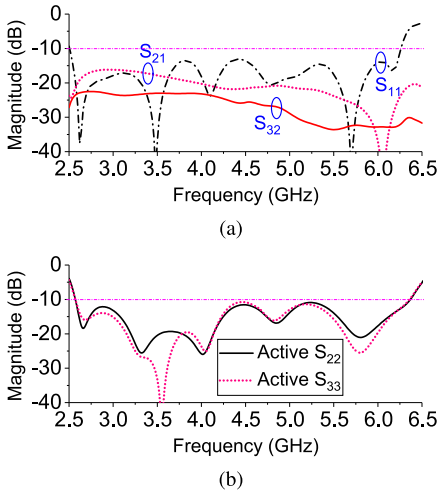

FIGURE 4. (a) Scattering parameters of the antenna array. (b) Active S_{22} when the two leftmost elements are excited and Active S_{33} when the two rightmost elements are excited.

The active reflection coefficient for the case where the two leftmost ports are excited is defined as follows.

$$\text{Active } S_{22} = \frac{S_{22} + S_{21}}{2}, \tag{1}$$

whereas the corresponding active reflection coefficient for the case where the two rightmost ports are excited can be written as

$$\text{Active } S_{33} = \frac{S_{33} - S_{31}}{2}, \tag{2}$$

The negative sign between S_{33} and S_{31} in (2) is due to the intrinsic phase inversion of the mirrored input transmission line connected to Port 3. Due to reciprocity, the Active S_{11} will be the same as Active S_{22} when the two leftmost elements are excited. Likewise, when the two rightmost elements are excited, the Active S_{11} will be the same as Active S_{33}.

B. SWITCHABLE POWER DIVIDER

To selectively excite the presented triple-element antenna by two in-phase inputs and one inactive input, a switchable power divider is proposed as illustrated in Fig. 5a. It is composed of two side-by-side Wilkinson power dividers [43] which are isolated from each other by sets of PIN 3 and PIN 4 diodes. The related dimensions of this power divider are summarized in Table 1. Port 2, Port 3 and Port 4 of this power divider are respectively connected to Port 2, Port 3, and Port 1 of the the antenna structure shown in Fig. 3a. The six PIN diodes in this structure are clustered into two groups denoted as PIN 3 and PIN 4. Each group is biased by one biasing voltage and the DC ground is the middle line of the power divider. The bias lines for these PIN diodes, each of which is connected to a 15 nH RF choke, are shown in Fig. 1b. The proposed PIN diode arrangement is used to enhance the isolation between the excited and inactive antenna elements. Two 100 Ω resistors are employed for the output isolation of the power divider.

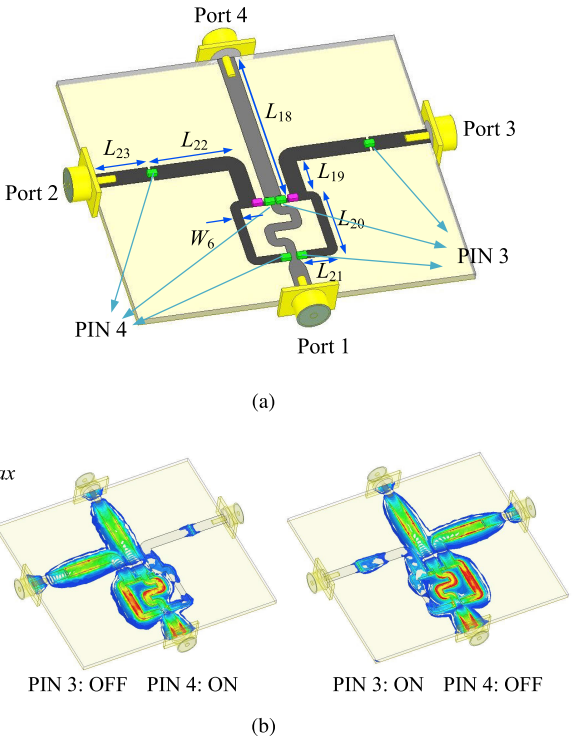

FIGURE 5. Three-way switchable power divider. (a) 3D view of the geometry with parameters defining the dimensions. (b) Instantaneous E-field distribution for the two states of the PIN diode switches.

The instantaneous electric field densities for the cases when each group of PIN diodes is switched ON are represented in Fig. 5b. The common middle output branch is always excited while either of the two lateral output branches can be selected. When PIN 3 diodes are switched ON and PIN 4 diodes are switched OFF simultaneously, the input signal splits between the middle and the right output branches. When PIN 4 diodes are switched ON and PIN 3 diodes are switched OFF simultaneously, the input signal splits between the middle and the left output branches.

To analyze the power divider performance, the transmission line model of the triple-output power divider is illustrated in Fig. 6. Equivalent models of the PIN diodes are used for this analysis. The 70.7 Ω transmission line lengths are set to be equal to a quarter wavelength at 4.2 GHz, i.e. near the middle of the wide operating bandwidth of the antenna.

The scattering parameters and the output phase difference of the Electromagnetic (EM) and circuit model of this power divider when the diodes PIN 4 are ON and the diodes PIN 3 are OFF are shown in Fig. 7. Due to the introduction of the PIN diodes in the circuit model of the triple-output Wilkinson power divider, the scattering performance is not ideal at the center frequency. In the EM model, bending and inevitable coupling of the transmission lines affect the scattering performances. This is the main reason behind the difference between the EM and circuit simulation results. Based on the EM and circuit simulation results, it is seen that the reflection coefficients are below −12 dB for the range of 2.5 GHz to 6.5 GHz. The transmission coefficient from

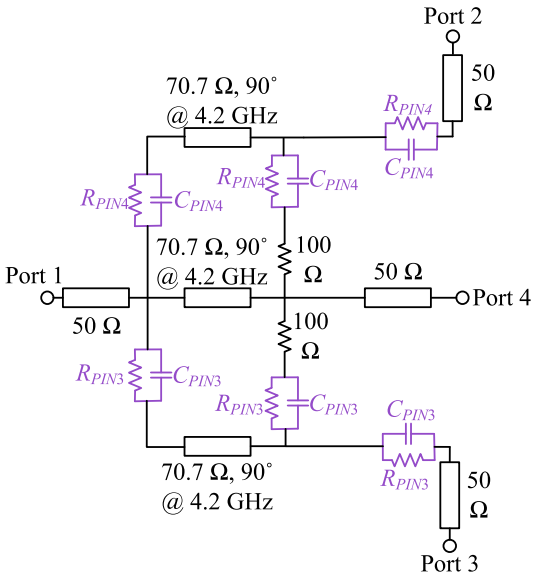

FIGURE 6. Circuit model of the presented power divider including the equivalent model of the PIN diodes.

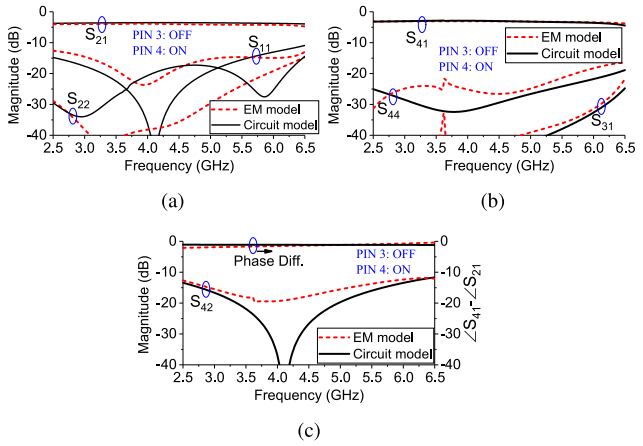

FIGURE 7. Scattering parameters calculated with the circuit model versus EM model of the power divider when PIN 3 diodes are OFF and PIN 4 diodes are ON. (a) S_{11}, S_{22}, and S_{21}. (b) S_{31}, S_{41}, and S_{44}. (c) S_{42} and the phase difference between the activated output ports.

Port 1 to Port 2 (S_{21}) and from Port 1 to Port 4 (S_{41}) are around −4 dB and −3 dB, respectively. The 1 dB transmission loss from Port 1 to Port 2 stems from the parasitic resistance of the PIN 4 diodes. This transmission loss is not present from Port 1 to Port 4 since there is no PIN diode between these two ports. The value of S_{31} is lower than −20 dB for the whole band demonstrating that only negligible power is transmitted to Port 3. The output phase difference in the EM simulation is varying from −2 degrees to 0 degrees, while the circuit simulation results exhibit constantly 0 degrees phase difference across this range. The isolation between the activated output ports (S_{42}) is below −12 dB from 2.5 GHz to 6.5 GHz. It will be demonstrated in section III that this value does not adversely affect the whole antenna system performance. The scattering parameters for the state when PIN 3 diodes are ON and PIN 4 diodes are OFF are identical to the state described above, with the only difference being that the input signal is equally split between Port 3 and Port 4 with no signal going to Port 2. Hence, these very similar results are not shown for brevity.

C. SWITCHABLE ALLPASS TO TUNABLE BANDPASS AND TUNABLE BANDSTOP FILTER

Based on the integration of the switchable power divider and the triple-element antenna, the sum and difference pattern diversity function is generated with wideband frequency response. To add the frequency selectivity function, a reconfigurable filter with switchable allpass to tunable bandpass/bandstop performance is required to feed the pattern reconfigurable antenna. While switchable and frequency-agile filters have widely been studied in the literature [44]–[49], a design which enables to switch between all three states of cognitive radio namely allpass, tunable bandpass, and tunable bandstop is lacking. Herein, allpass functionality is added to the tunable bandpass-to-bandstop filter formerly presented in [31]. The filter structure is depicted in Fig. 8a including two sets of PIN diodes namely PIN 1 and PIN 2 and two varactor diodes. PIN 2 diodes are switched ON or OFF together and the two varactors are biased with the same voltage. The dimensions of this filter are summarized in Table 1. For simplicity and clarity, the bias lines, choke inductors and DC block capacitors are not shown in Fig. 8a. However, they are displayed in the reconfigurable filter structure depicted in Fig. 1c. To bias the PIN and varactor diodes in the filter design, five inductors are connected to the DC bias lines, while one inductor is connected to the bottom layer of the filter which is RF and DC ground. This short-ended inductor provides a DC ground path for PIN 1 diode. Two DC block capacitors (visible in Fig. 1a) are used in the narrow coupled line of the reconfigurable filter to avoid the DC current of the PIN 2 diode to mix with the DC current of the varactors.

The instantaneous electric field density at the lowest passband and the frequency response of the reconfigurable filter in bandpass state are shown in Fig. 8b. In this state, all the PIN diodes are OFF and by changing the varactor capacitance, the operating frequency changes. The working principle in this case is that when PIN 1 diode is OFF, there is no direct path from input port to the output port. The input signal will pass through the narrow coupled line at a specific resonance frequency, which depends on the varactors capacitance thus generating a bandpass filtering response with tunable frequency. The PIN 2 diodes are OFF in this tunable bandpass state to allow the signal to pass through the narrow coupled line.

The instantaneous electric field density at the lowest notch band and the frequency response for the reconfigurable bandstop filtering state are shown in Fig. 8c. In this state, PIN 1 is switched ON providing a direct path for the input signal to reach the output. Nevertheless, the narrow coupled line will block this path at a specific resonance frequency which is tuned by varying the varactors capacitance. The PIN 2 diodes are switched OFF in this tunable bandstop filtering state.

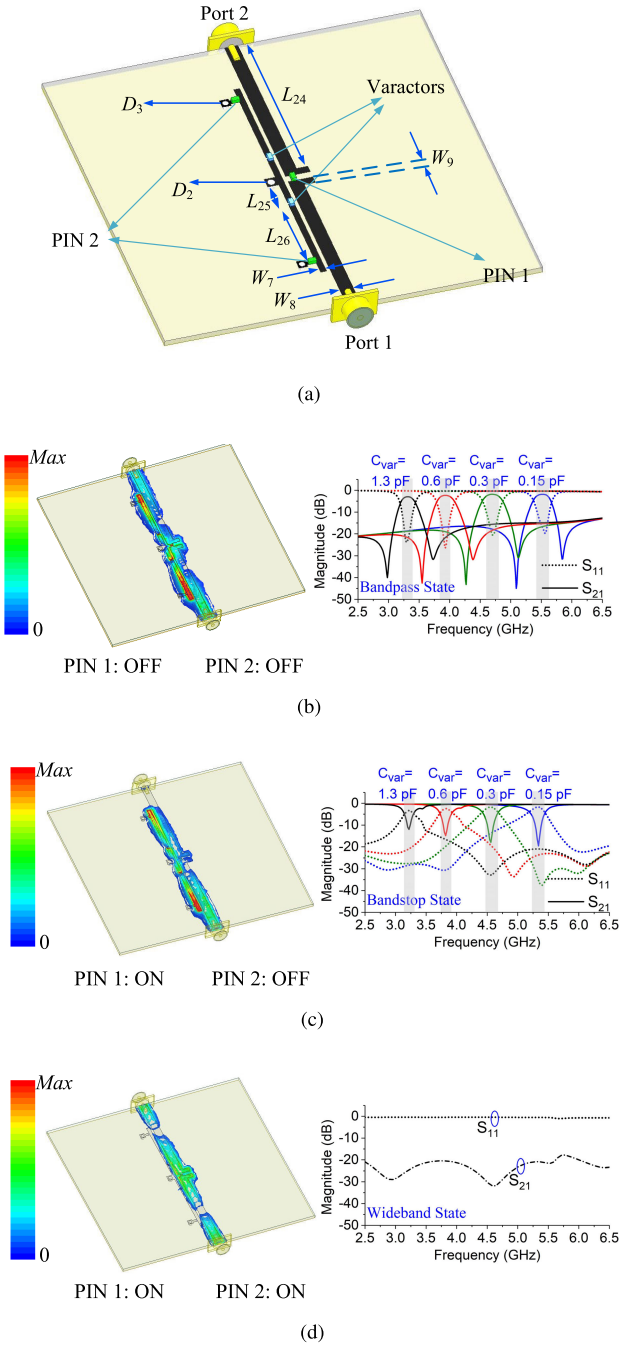

FIGURE 8. Proposed reconfigurable three-state filter. (a) 3D view and the related dimensions. (b) Passband E-field distribution at 3.3 GHz and simulated scattering parameters for bandpass state. (c) notch-band E-field distribution at 3.2 GHz and simulated scattering parameters for the bandstop state. (d) E-field distribution at 3.5 GHz and simulated scattering parameters for allpass filtering state.

This, in turn, allows the narrow coupled line to create a notch frequency.

Given that the narrow coupled transmission line plays a key role in transmitting and blocking the input signal to the output port for the bandpass and bandstop states, respectively, neutralizing its effect can provide another operation state of allpass filtering response. This state is illustrated in Fig. 8d,

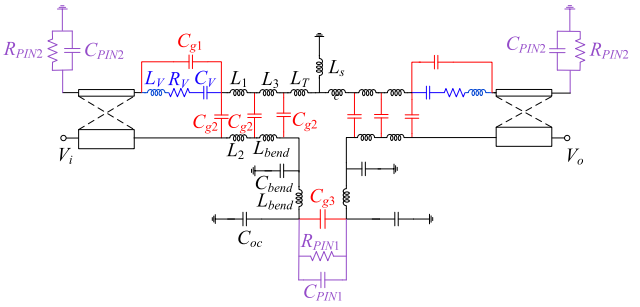

FIGURE 9. Equivalent circuit model of the filter.

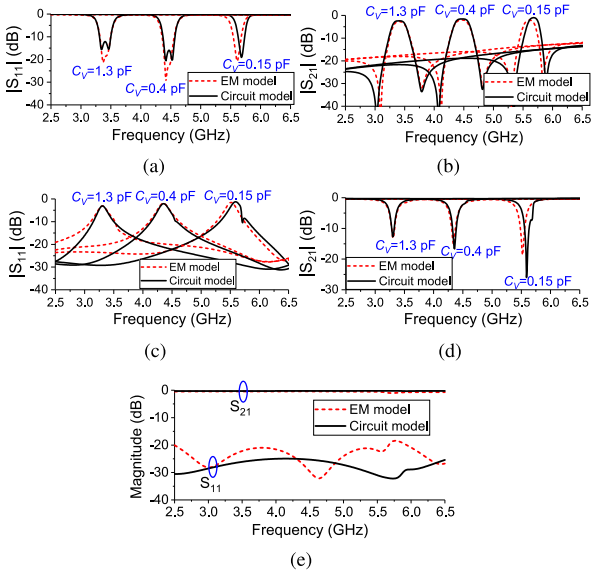

FIGURE 10. Scattering parameters of EM model versus circuit model of the filter. (a) S_{11} of the tunable bandpass state. (b) S_{21} of the tunable bandpass state. (c) S_{11} of the tunable bandstop state. (d) S_{21} of the tunable bandstop state. (e) S_{11} and S_{21} of the wideband state.

where the PIN 1 diode is switched ON to provide a path from input to the output, while the short-ended PIN 2 diodes are switched ON to connect the narrow coupled line to the ground plane, thus neutralizing its effect. To minimize the power dissipation, no bias voltage is applied to the varactors in this state. The whole filter structure will be simplified to a 50 Ω transmission line in this state. Feeding inherently wideband antennas by this 50 Ω transmission line will result in a wideband response for the whole system. This wideband response is useful for the spectrum sensing case in cognitive radio systems, i.e. as an important state of operation missing in [31]. Therefore, the newly proposed change in the structure will bring about a substantial improvement in the response of the overall system.

To analyze the filter performance, the behavior of its equivalent circuit model depicted in Fig. 9 is studied in the following. The distributed coupling capacitors are in red, the varactor equivalent elements are in blue and the PIN diode equivalent elements are in purple. When PIN 2 diodes are OFF, the equivalent model will behave the same way as the bandpass/bandstop filter presented in [31] with the same values of the lumped elements. The EM and circuit simulation results

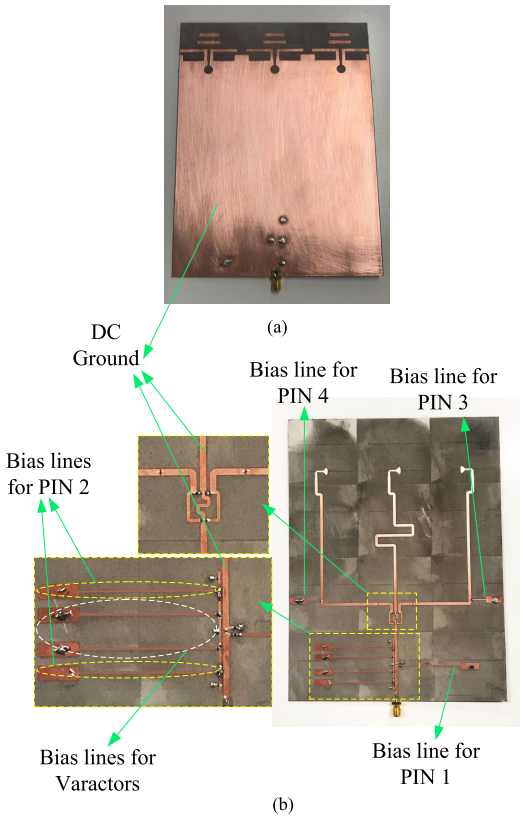

FIGURE 11. Photograph of the fabricated antenna. (a) Bottom layer. (b) Top layer with magnified feeding network.

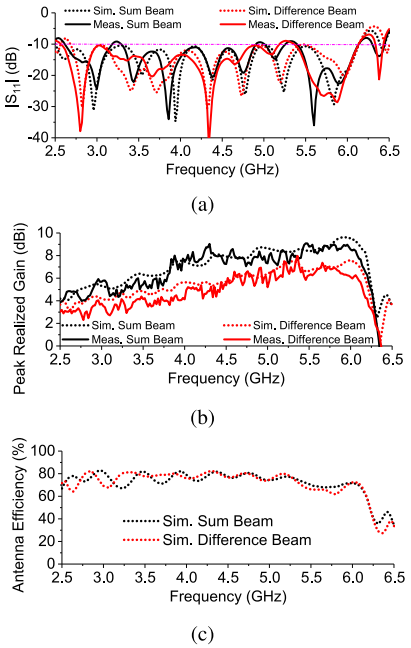

FIGURE 12. Frequency responses of the proposed antenna in the wideband state with sum and difference radiation patterns. (a) Reflection coefficient. (b) Maximum realized gain. (c) Total antenna efficiency.

of the bandpass state are illustrated in Fig. 10a and Fig. 10b. In this state, because PIN 1 is OFF, the coupling capacitors provide a path between input and output at the resonance

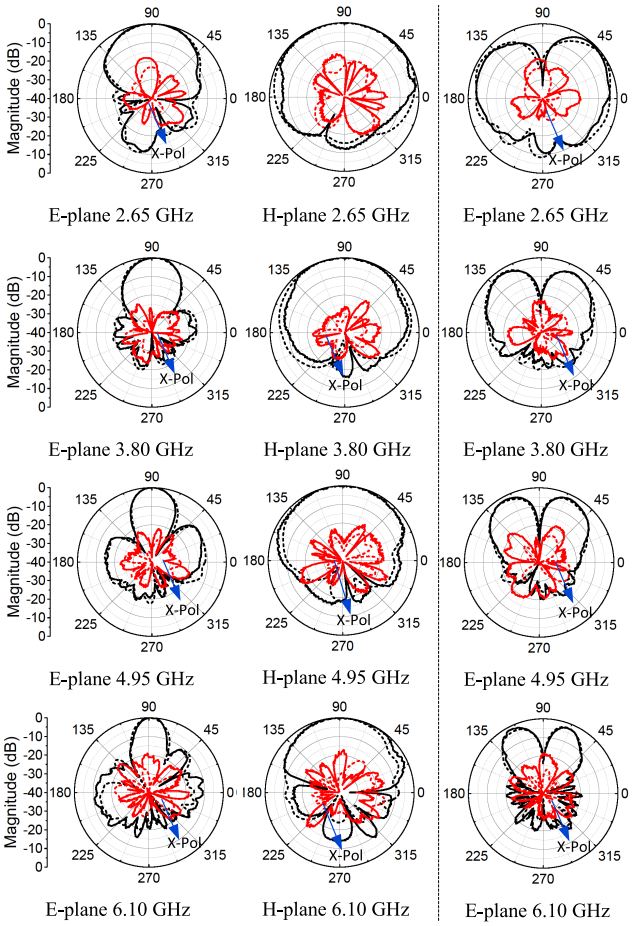

FIGURE 13. Measured and simulated radiation patterns at different frequencies for the wideband state of operation. Left column: E-plane radiation pattern for the sum beam operation. Middle column: H-plane radiation pattern for the sum beam operation. Right column: E-plane radiation pattern for the difference beam operation.

frequency which is controlled by tuning the varactors. The EM versus circuit simulation results for the bandstop state are illustrated in Fig. 10c and Fig. 10d. In this state, PIN 1 is ON and the coupling capacitors take the opposite role, namely blocking the input signal to the output port at the resonance frequency which can be controlled by tuning the varactors. The last state of filter operation which distinguishes this filter from the one presented in [31] occurs when PIN 2 diode is ON. In this state, the effect of the distributed coupling capacitors is mitigated and the filter will turn into an allpass design when PIN 1 is ON. The EM and circuit simulation results for the allpass state are illustrated in Fig. 10e.

III. MEASUREMENT RESULTS

After integration of all the antenna components, the states of PIN and varactor diodes determine the overall system states as summarized in Table 2. Based on the proposed design refined through EM simulations, the antenna system has been fabricated and a photograph of the prototype is shown in Fig. 11. The total substrate volume is

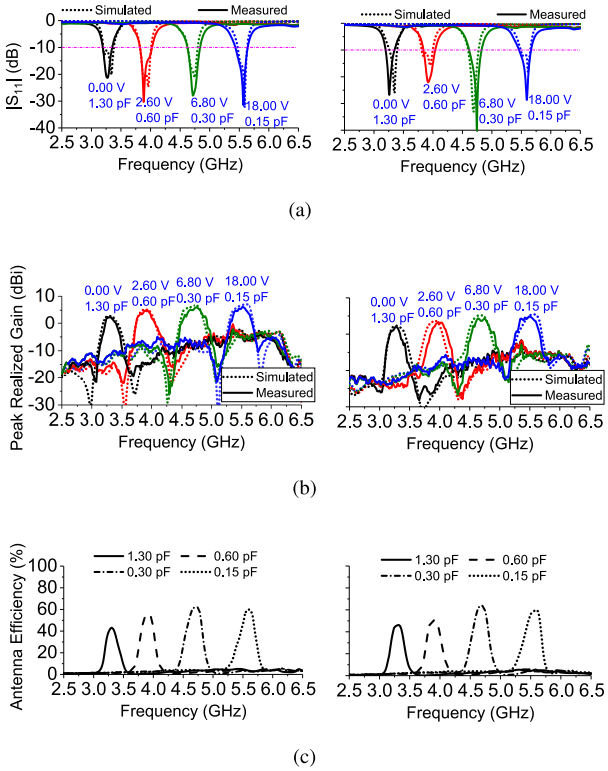

FIGURE 14. Frequency responses of the proposed antenna in the bandpass state. Left column: sum beam operation. Right column: difference beam operation. (a) Reflection coefficient. (b) Maximum realized gain. (c) Total antenna efficiency.

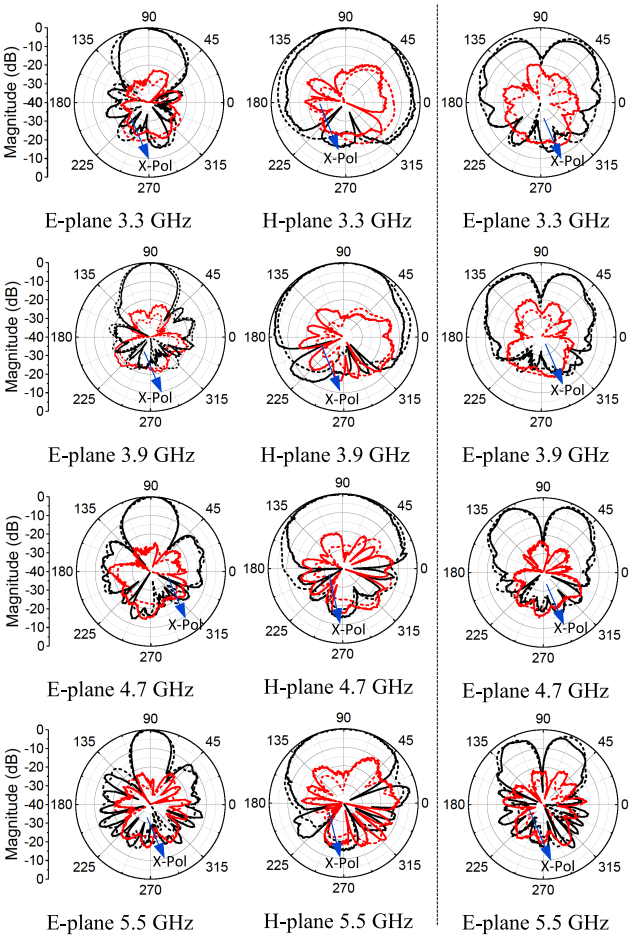

FIGURE 15. Measured and simulated radiation patterns at different frequencies for the bandpass state of operation. Left column: E-plane radiation pattern for the sum beam operation. Middle column: H-plane radiation pattern for the sum beam operation. Right column: E-plane radiation pattern for the difference beam operation.

$W \times L \times H = 144 \times 190 \times 0.8182$ mm^3 corresponding to $1.24\lambda_0 \times 1.65\lambda_0 \times 0.007\lambda_0$ where λ_0 is the wavelength at the lowest operating frequency. There are seven biasing lines in the fabricated prototype which are AC-isolated from the antenna structure by seven RF chokes at the end of each line. The DC grounds are the antenna bottom layer as well as the antenna middle feeding line. It is noteworthy that the gaps used for mounting lumped elements are all 0.3 mm wide.

A. WIDEBAND OPERATION STATE

According to Table 2, when PIN 1 and PIN 2 diodes are both switched ON and no voltage is applied to the varactors, the filter is in allpass state. This case is analogous to exciting the wideband pattern switchable antenna array by a 50 Ω transmission line. Hence, the wideband operation state for the whole system is activated. The reflection coefficients are illustrated in Fig. 12a with the simulated (measured) overlapping bandwidth for the sum and difference beams extending from 2.68 GHz (2.62 GHz) to 6.10 GHz (6.10 GHz). This corresponds to 77.9% (79.8%) fractional bandwidth with minor breaches of the −10 dB specification in the measured data. The simulated (measured) maximum realized gain of the antenna illustrated in Fig. 12b is varying from 4.8 dBi (4.8 dBi) to 8.7 dBi (7.7 dBi) for the sum beam pattern, while it is varying from 3.8 dBi (3.0 dBi) to 6.8 dBi (5.7 dBi) for the difference beam pattern. The simulated antenna efficiency is more than 62.0% within the whole bandwidth as represented in Fig. 12c. The simulated and measured sum and difference radiation patterns at four sample frequencies are plotted in Fig. 13.

TABLE 2. Switching Patterns and the Different Frequency Operation States.

PIN 1	PIN 2	PIN 3	PIN 4	Varactors	Behavior
ON	ON	ON	OFF	1.3 pF	WB / Difference
ON	ON	OFF	ON	1.3 pF	WB / Sum
OFF	OFF	ON	OFF	0.15 pF to 1.3 pF	Tunable BP / Difference
OFF	OFF	OFF	ON	0.15 pF to 1.3 pF	Tunable BP / Sum
ON	OFF	ON	OFF	0.15 pF to 1.3 pF	Tunable BS / Difference
ON	OFF	OFF	ON	0.15 pF to 1.3 pF	Tunable BS / Sum

WB: Wideband, BP: Bandpass, BS: Bandstop

B. BANDPASS OPERATION STATE

The tunable bandpass state of operation occurs when both PIN 1 and PIN 2 diodes are switched OFF and the varactor capacitances are controlled by the tuning bias voltage. In this state, the whole system takes on the frequency

TABLE 3. Comparison of the proposed antenna system with some recently published antennas featuring tunable filtering response.

Refs.	ε_r	Size $(\lambda_0)^3$	Mode of Operation			Reconfigurable Patterns	Pattern Type	In-built Phase Inverter
			Wideband (BW)	Tunable BP (TR)	Tunable BS (TR)			
[27]	2.2	0.72×0.30×0.01	✓ (44.9%)	✓ (21.0%)	✗	✗	omnidirectional	✗
[29]	3.48	0.39×0.23×0.011	✓ (71.7%)	✓ (36.0%)	✗	✗	omnidirectional	✗
[30]	2.2	0.42×0.3×0.002	✗	✓* (57.0%)	✓ (57.0%)	✗	omnidirectional	✗
[31]	3.38	0.75×0.7×0.008	✗	✓ (50.0%)	✓ (50.4%)	✗	sum and difference (two-port)	✗
[37]	3.0	1.21×1.21×0.17	✓ (60.2%)	✗	✗	✓	broadside to conical	✗
This Work	3.38	1.24×1.65×0.007	✓ (79.8%)	✓ (51.3%)	✓ (50.3%)	✓	sum and difference	✓

BW: Bandwidth, BP: Bandpass, BS: Bandstop, TR: Tuning Range
* No experimental validation for bandpass case is provided in this reference.

characteristic of the tunable bandpass filter. Based on the simulated (measured) reflection coefficient plots in Fig. 14a, the operating frequency can be tuned from 3.30 GHz (3.28 GHz) to 5.58 GHz (5.55 GHz) corresponding to a tuning range of 51.3% (51.3%). This value is roughly the same for both cases of sum and difference radiation patterns. Within this tuning range, the simulated (measured) maximum realized gain illustrated in Fig. 14b is varying from 2.9 dBi (2.4 dBi) to 7.0 dBi (6.0 dBi) for the sum beam case, while it is varying from 2.2 dBi (1.9 dBi) to 5.4 dBi (4.4 dBi) for the difference beam case. The simulated antenna efficiencies for both sum and difference radiation patterns are shown in Fig. 14c with the minimum value of 46.0% observed at the lowest operating frequencies, which is typical for varactor controlled frequency-tunable antennas. This value increases with raising tuning frequencies and this effect is attributed to the parasitic resistance of the varactor diode. The simulated and measured radiation patterns within the passbands of the tunable bandpass antenna are shown in Fig. 15.

C. BANDSTOP OPERATION STATE

Referring to Table 2, when PIN 1 is switched ON and PIN 2 is switched OFF, the bandstop operation state is activated and the notched frequency is tuned by varying the bias voltage controlling the varactor capacitances. In this state, the frequency response of the whole systems takes on the characteristics of the tunable bandstop filter. It is seen in Fig. 16a that the simulated (measured) notched frequency can be tuned from 3.20 GHz (3.20 GHz) to 5.40 GHz (5.35 GHz) corresponding to a tuning range of 51.1% (50.3%) for the sum pattern and it is nearly the same for the difference beam pattern. Moreover, the simulated (measured) maximum realized gain attenuation within the notch-bands is higher than 13.0 dBi (10.4 dBi) for both the sum and difference radiation patterns based on Fig. 16b. As the varactor capacitance decreases, the attenuation level increases. The simulated antenna efficiencies for the sum and difference beams are illustrated in Fig. 16c. For both the sum and difference beams, the total antenna efficiency at the notch frequencies becomes well below 10.0% for the whole tuning range, thus lowering the realized gain. The simulated and measured out-of-band radiation patterns for the tunable bandstop state are similar to the wideband counterparts. Hence, for brevity they are not shown here.

D. COMPARISON WITH RECENTLY PUBLISHED DESIGNS

The performance of the proposed design is compared in Table 3 with some recently published designs featuring switchable and continuously tunable frequency performances. For better comparison, the selected references are all exhibiting continuous tunability in their narrowband states. It is observed that the proposed design is the only design generating all three states of wideband, tunable bandpass, and tunable bandstop performance. In contrast to the designs presented in [31] and [37] where sum and difference patterns were realized by an external coupler and a switchable ultra-wideband phase inverter, respectively, the proposed design yields the sum and difference radiation patterns using an in-built phase inverter in the antenna structure, thus reducing the complexity of the feeding network. The large dimensions of the proposed design compared to the other references and sequential pattern switching compared to double-input pattern diversity antennas are the only sacrificed features to obtain this unique functionality.

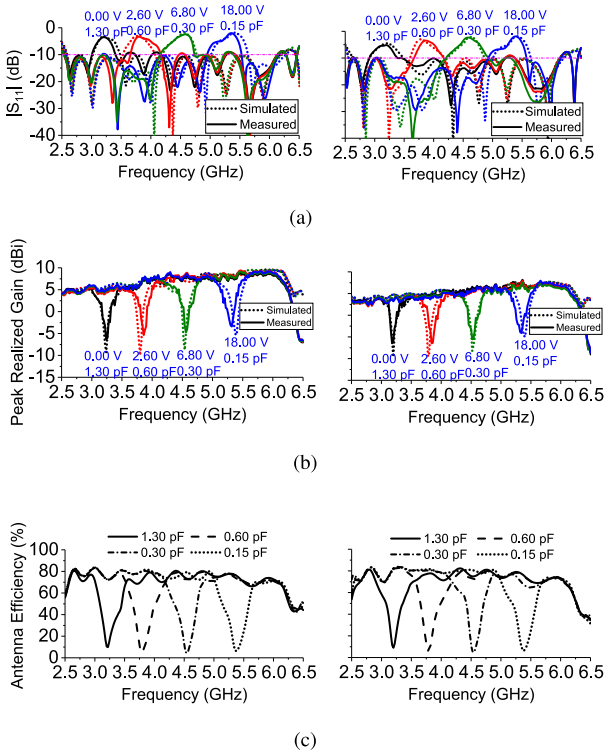

FIGURE 16. Frequency responses of the proposed antenna in the bandstop state. Left column: sum beam operation. Right column: difference beam operation. (a) Reflection coefficient. (b) Maximum realized gain. (c) Total antenna efficiency.

IV. CONCLUSION

In this paper, the design of a sum and difference pattern-reconfigurable antenna with three switchable states of wideband, tunable bandstop, and tunable bandpass operation has been presented. This antenna system has been developed by integration of a switchable and tunable filter, a modified switchable power divider, and a triple-element quasi Yagi-Uda antenna array with an in-built phase inverter. The simulation and measurement results have shown that this design can successfully achieve wideband operation with a bandwidth of 79.8%, which can be switched to a tunable bandpass and tunable bandstop with 51.3% and 50.3% tuning range, respectively. The results also demonstrated that the system can switch between the sum and difference beam radiation patterns by exploiting its in-built phase inverter while working in each of the switchable filtering states.

REFERENCES

[1] Y. Tawk, A. El-Amine, S. Saab, J. Costantine, F. Ayoub, and C. G. Christodoulou, "A software-defined frequency-reconfigurable meandered printed monopole," *IEEE Antennas Wireless Propag. Lett.*, vol. 17, no. 2, pp. 327–330, Feb. 2018.

[2] M. Shirazi, J. Huang, T. Li, and X. Gong, "A switchable-frequency slot-ring antenna element for designing a reconfigurable array," *IEEE Antennas Wireless Propag. Lett.*, vol. 17, pp. 229–233, Feb. 2018.

[3] Y.-M. Cai, K. Li, Y. Yin, S. Gao, W. Hu, and L. Zhao, "A low-profile frequency reconfigurable grid-slotted patch antenna," *IEEE Access*, vol. 6, pp. 36305–36312, 2018.

[4] F. Sun, F.-S. Zhang, H. Zhang, H. Zhang, C. Li, and C. Feng, "A frequency diversity printed-Yagi antenna element for apertures selectivity wideband array application," *IEEE Trans. Antennas Propag.*, vol. 66, no. 10, pp. 5634–5638, Oct. 2018.

[5] S.-A. Malakooti and C. Fumeaux, "Dual-band bandpass filtering monopole antenna with independently tunable frequencies," in *Proc. IEEE Asia–Pacific Conf. Antennas Propag.*, Incheon, South Korea, Aug. 2019, pp. 1–2.

[6] M. S. Alam and A. M. Abbosh, "Wideband pattern-reconfigurable antenna using pair of radial radiators on truncated ground with switchable director and reflector," *IEEE Antennas Wireless Propag. Lett.*, vol. 16, pp. 24–28, 2017.

[7] Y. Tawk, J. Costantine, and C. G. Christodoulou, "An eight-element reconfigurable diversity dipole system," *IEEE Trans. Antennas Propag.*, vol. 66, no. 2, pp. 572–581, Feb. 2018.

[8] G. Jin, M. Li, L. Dan, and G. Zeng, "A simple planar pattern-reconfigurable antenna based on arc dipoles," *IEEE Antennas Wireless Propag. Lett.*, vol. 17, no. 9, pp. 1664–1668, Sep. 2018.

[9] S.-L. Chen, P.-Y. Qin, W. Lin, and Y. J. Guo, "Pattern-reconfigurable antenna with five switchable beams in elevation plane," *IEEE Antennas Wireless Propag. Lett.*, vol. 17, no. 3, pp. 454–457, Mar. 2018.

[10] A. Panahi, X. L. Bao, K. Yang, O. O'Conchubhair, and M. J. Ammann, "A simple polarization reconfigurable printed monopole antenna," *IEEE Trans. Antennas Propag.*, vol. 63, no. 10, pp. 5129–5164, Nov. 2015.

[11] H. Sun and S. Sun, "A novel reconfigurable feeding network for quad-polarization-agile antenna design," *IEEE Trans. Antenna Propag.*, vol. 64, no. 1, pp. 311–316, Jan. 2016.

[12] J.-S. Row and Y.-H. Wei, "Wideband reconfigurable crossed-dipole antenna with quad-polarization diversity," *IEEE Trans. Antennas Propag.*, vol. 66, no. 4, pp. 2090–2094, Apr. 2018.

[13] F. F. Farzami, S. Khaledian, B. Smida, and D. Erricolo, "Reconfigurable linear/circular polarization rectangular waveguide filtenna," *IEEE Trans. Antennas Propag.*, vol. 66, no. 1, pp. 9–15, Jan. 2018.

[14] N. Nguyen-Trong, L. Hall, and C. Fumeaux, "A frequency- and polarization-reconfigurable stub-Loaded microstrip patch antenna," *IEEE Trans. Antennas Propag.*, vol. 63, no. 11, pp. 5235–5240, Nov. 2015.

[15] L.-R. Tan, R.-X. Wu, and Y. Poo, "Magnetically reconfigurable SIW antenna with tunable frequencies and polarizations," *IEEE Trans. Antennas Propag.*, vol. 63, no. 6, pp. 2772–2776, Jun. 2015.

[16] P. K. Li, Z. H. Shao, Q. Wang, and Y. J. Cheng, "Frequency- and pattern-reconfigurable antenna for multistandard wireless applications," *IEEE Antennas Wireless Propag. Lett.*, vol. 14, pp. 333–336, 2014.

[17] N. Nguyen-Trong, L. Hall, and C. Fumeaux, "A frequency- and pattern-reconfigurable center-shorted microstrip antenna," *IEEE Antennas Wireless Propag. Lett.*, vol. 15, pp. 1955–1958, 2016.

[18] S.-L. Chen, P.-Y. Qin, C. Ding, and Y. J. Guo, "Cavity-backed proximity-coupled reconfigurable microstrip antenna with agile polarizations and steerable beams," *IEEE Trans. Antennas Propag.*, vol. 65, no. 10, pp. 5553–5558, Oct. 2017.

[19] J. Hu and Z.-C. Hao, "A compact polarization-reconfigurable and 2-D beam-switchable antenna using the spatial phase shift technique," *IEEE Trans. Antennas Propag.*, vol. 66, no. 10, pp. 4986–4995, Oct. 2018.

[20] Y. Tawk, J. Costantine, and C. G. Christodoulou, "Cognitive-radio and antenna functionalities: A tutorial," *IEEE Antennas Propag. Mag.*, vol. 56, no. 1, pp. 231–243, Feb. 2014.

[21] E. Ebrahimi, J. R. Kelly, and P. S. Hall, "Integrated wide-narrowband antenna for multi-standard radio," *IEEE Trans. Antennas Propag.*, vol. 59, no. 7, pp. 2628–2635, Jul. 2011.

[22] M. R. Hamid, P. Gardner, P. S. Hall, and F. Ghanem, "Switched-band Vivaldi antenna," *IEEE Trans. Antennas Propag.*, vol. 59, no. 5, pp. 1472–1480, May 2011.

[23] M. R. Hamid, P. Gardner, P. S. Hall, and F. Ghanem, "Vivaldi antenna with integrated switchable band pass resonator," *IEEE Trans. Antennas Propag.*, vol. 59, no. 11, pp. 4008–4015, Nov. 2011.

[24] J. Deng, S. Hou, L. Zhao, and L. Guo, "A reconfigurable filtering antenna with integrated bandpass filters for UWB/WLAN applications," *IEEE Trans. Antennas Propag.*, vol. 66, no. 1, pp. 401–404, Jan. 2018.

[25] E. Erfani, J. Nourinia, C. Ghobadi, M. Niroo-Jazi, and T. A. Denidni, "Design and implementation of an integrated UWB/reconfigurable-slot antenna for cognitive radio applications," *IEEE Antennas Wireless Propag. Lett.*, vol. 11, pp. 77–80, 2012.

[26] A. Mansoul, F. Ghanem, M. R. Hamid, and M. Trabelsi, "A selective frequency-reconfigurable antenna for cognitive radio applications," *IEEE Antennas Wireless Propag. Lett.*, vol. 13, pp. 515–518, 2014.

[27] P.-Y. Qin, F. Wei, and Y. J. Guo, "A wideband-to-narrowband tunable antenna using a reconfigurable filter," *IEEE Trans. Antennas Propag.*, vol. 63, no. 5, pp. 2282–2285, May 2015.
[28] L. Ge and K. M. Luk, "Band-reconfigurable unidirectional antenna: A simple, efficient magneto-electric antenna for cognitive radio applications," *IEEE Antennas Propag. Mag.*, vol. 58, no. 2, pp. 18–27, Apr. 2016.
[29] M.-C. Tang, Z. Wen, H. Wang, M. Li, and R. W. Ziolkowski, "Compact, frequency-reconfigurable filtenna with sharply defined wideband and continuously tunable narrowband states," *IEEE Trans. Antennas Propag.*, vol. 65, no. 10, pp. 5026–5034, Oct. 2017.
[30] A. K. Horestani, Z. Shaterian, J. Naqui, F. Martín, and C. Fumeaux, "Reconfigurable and tunable S-shaped split-ring resonators and application in band-notched UWB antennas," *IEEE Trans. Antennas Propag.*, vol. 64, no. 9, pp. 3766–3776, Sep. 2016.
[31] S.-A. Malakooti, S. M. H. Mousavi, and C. Fumeaux, "Tunable bandpass-to-bandstop quasi-Yagi–Uda antenna with sum and difference radiation patterns," *IEEE Trans. Antennas Propag.*, vol. 67, no. 4, pp. 2260–2271, Apr. 2019.
[32] Y. Dong and T. Itoh, "Planar ultra-wideband antennas in Ku- and K-band for pattern or polarization diversity applications," *IEEE Trans. Antennas Propag.*, vol. 60, no. 6, pp. 2886–2895, Jun. 2012.
[33] Y.-W. Wang, G.-M. Wang, Z.-W. Yu, J.-G. Liang, and X.-J. Gao, "Ultra-wideband *E*-plane monopulse antenna using Vivaldi antenna," *IEEE Trans. Antennas Propag.*, vol. 62, no. 10, pp. 4961–4969, Oct. 2014.
[34] S.-A. Malakooti, M. Moosazadeh, D. C. Ranasinghe, and C. Fumeaux, "Antipodal Vivaldi antenna for sum and difference radiation patterns with reduced grating lobes," *IEEE Antennas Wireless Propag. Lett.*, vol. 16, pp. 3139–3142, 2017.
[35] Y. Dong, J. Choi, and T. Itoh, "Vivaldi antenna with pattern diversity for 0.7 to 2.7 GHz cellular band applications," *IEEE Antennas Wireless Propag. Lett.*, vol. 17, no. 2, pp. 247–250, Feb. 2018.
[36] Z.-C. Hao, H.-H. Wang, and W. Hong, "A novel planar reconfigurable monopulse antenna for indoor smart wireless access points' application," *IEEE Trans. Antennas Propag.*, vol. 64, no. 4, pp. 1250–1260, Apr. 2016.
[37] X. Yang, H. Lin, H. Gu, L. Ge, and X. Zeng, "Broadband pattern diversity patch antenna with switchable feeding network," *IEEE Access*, vol. 6, pp. 69612–69619, 2018.
[38] M/A-COM. (2019). *Products: MA4FCP300*. [Online]. Available: https://cdn.macom.com/datasheets/MA4FCP300.pdf
[39] M/A-COM. (2019). *Products: MA46H120*. [Online]. Available: https://cdn.macom.com/datasheets/MA46H120Series.pdf
[40] Murata. (2019). *Products: LQW15AN15NG00*. [Online]. Available: https://psearch.en.murata.com/inductor/product/LQW15AN15NG00%23.pdf
[41] Murata. (2019). *Products: GRM0332C1H100JA01*. [Online]. Available: https://psearch.en.murata.com/capacitor/product/GRM0332C1H100JA01%23.pdf
[42] J. Wu, Z. Zhao, Z. Nie, and Q.-H. Liu, "Bandwidth enhancement of a planar printed quasi-Yagi antenna with size reduction," *IEEE Trans. Antennas Propag.*, vol. 62, no. 1, pp. 463–467, Jan. 2014.
[43] E. J. Wilkinson, "An N-way hybrid power divider," *Proc. IRE*, vol. 8, no. 1, pp. 116–118, Jan. 1960.
[44] E. J. Naglich, J. Lee, D. Peroulis, and W. J. Chappell, "A tunable bandpass-to-bandstop reconfigurable filter with independent bandwidths and tunable response shape," *IEEE Trans. Microw. Theory Techn.*, vol. 58, no. 12, pp. 3770–3779, Dec. 2010.
[45] J. Lee, E. J. Naglich, H. H. Sigmarsson, D. Peroulis, and W. J. Chappell, "New bandstop filter circuit topology and its application to design of a bandstop-to-bandpass switchable filter," *IEEE Trans. Microw. Theory Techn.*, vol. 61, no. 3, pp. 1114–1123, Mar. 2013.
[46] Y.-H. Cho and G. M. Rebeiz, "0.7–1.0-GHz reconfigurable bandpass-to-bandstop filter with selectable 2- and 4-pole responses," *IEEE Trans. Microw. Theory Techn.*, vol. 62, no. 11, pp. 2626–2632, Nov. 2014.
[47] Y.-H. Cho and G. M. Rebeiz, "Two- and four-pole tunable 0.7–1.1-GHz bandpass-to-bandstop filters with bandwidth control," *IEEE Trans. Microw. Theory Techn.*, vol. 62, no. 3, pp. 457–463, Mar. 2014.
[48] T. Yang and G. M. Rebeiz, "Bandpass-to-bandstop reconfigurable tunable filters with frequency and bandwidth controls," *IEEE Trans. Microw. Theory Techn.*, vol. 65, no. 7, pp. 2288–2297, Jul. 2017.
[49] F.-C. Chen, R.-S. Li, and J.-P. Chen, "A tunable dual-band bandpass-to-bandstop filter using p-i-n diodes and varactors," *IEEE Access*, vol. 6, pp. 46058–46065, 2018.

SEYED-ALI MALAKOOTI (S'18) received the B.S. and M.S. degrees in electrical and electronics engineering, in 2010 and 2013, respectively. He is currently pursuing the Ph.D. degree with The University of Adelaide.

His current research interest includes reconfigurable and pattern diversity antennas. He was a recipient of the Adelaide Scholarship International (ASI) from The University of Adelaide, in 2016. He received the Best (Platinum) Student Paper Award at the IEEE Asia-Pacific Conference on Antennas and Propagation (APCAP) 2019, Incheon, South Korea and the second prize at APCAP 2018, Auckland, New Zealand. He has served as a Reviewer for the IEEE Transactions on Microwave Theory and Techniques, the IEEE Microwave and Wireless Components Letters, the IEEE Antennas and Wireless Propagation Letters, IEEE Access, *IET Microwave and Antennas Propagation Letters*, and *IET Electronics letters*.

CHRISTOPHE FUMEAUX (M'03–SM'09–F'19) received the Diploma and Ph.D. degrees in physics from ETH Zurich, Switzerland, in 1992 and 1997, respectively.

From 1998 to 2000, he was a Postdoctoral Researcher with the School of Optics, University of Central Florida, Orlando, FL, USA. In 2000, he joined Swiss Federal Office of Metrology as a Scientific Staff Member. From 2001 to 2008, he was a Research Associate and a Lecturer with the Laboratory for Electromagnetic Fields and Microwave Electronics, ETH Zurich. Since 2008, he has been with The University of Adelaide, where he is currently a Professor with the School of Electrical and Electronic Engineering. His current research interests include concern antenna engineering, THz technology, and the application of RF design principles to optical micro/nano-structures. From 2011 to 2015, he was a Future Fellow of the Australian Research Council. He was a recipient of the ETH Medal for his doctoral dissertation. He was also a recipient of the 2018 Edward E. Altshuler Prize, the 2014 IEEE Sensors Journal, and the 2004 *ACES Journal* best paper awards. He also received best conference paper awards at the 2012 Asia-Pacific International Symposium on Electromagnetic Compatibility (APEMC 2012) and the 17th Colloque International sur la compatibilité Electromagnétique (CEM 2014). He was a recipient of The University of Adelaide Stephen Cole the Elder Award for Excellence in higher degree by Research Supervisory Practice, in 2018. Several of his students have received student awards with joint articles, including IMS 2006 and 2007, iWAT 2014, AMS 2014, the IEEE Australia Council 2014, NEMO 2015, ICEAA 2015 and 2016, ASA 2017, RADIO 2018, and APCAP 2018 and 2019. He served as an Associate Editor for the IEEE Transactions on Microwave Theory and Techniques, from 2010 to 2013. From 2013 to 2016, he served as a Senior Associate Editor and later the Associate Editor-in-Chief for the IEEE Transactions on Antennas and Propagation. Since March 2017, he has been serving as the Editor-in-Chief for the IEEE Antennas and Wireless Propagation Letters.